

Final Report: Advanced Image Restoration and Feature Extraction from Degraded Aerial Imagery

Lee Kyuho

Department of Computer Science and Engineering

Korea University

XAI507: Computer Vision and AI, Fall 2025

kyuholee@korea.ac.kr

1. Introduction

Aerial imagery is widely used in urban mapping, infrastructure monitoring, and autonomous navigation, but its quality is often degraded by atmospheric blur, sensor noise, and low contrast. To ensure reliable interpretation, a robust restoration and enhancement pipeline is required.

This project develops a three-stage framework for restoring degraded aerial images: (1) periodic noise removal using FFT-based frequency-domain filtering, (2) deblurring via Wiener deconvolution, and (3) contrast enhancement through histogram equalization. Quantitative metrics such as PSNR and SSIM are used to evaluate performance and determine the optimal processing order.

After restoration, edge and line detection are applied to extract structural features such as road boundaries and intersections. The comparison between degraded and restored images shows clear improvements in line detection robustness and network continuity, demonstrating the effectiveness of the proposed pipeline.

Overall, this work provides an interpretable framework for recovering both perceptual and structural fidelity in degraded aerial imagery and offers practical guidance for future preprocessing pipelines in aerial image analysis.

2. Methods

2.1. Image Degradation Simulation

A clean aerial image from the Inria Aerial Image Labeling Dataset was artificially degraded to simulate real-world distortions, and the image was slightly cropped for better analytical clarity. Three sequential degradations were applied:

- **Blur:** A Gaussian blur (11×11 kernel, $\sigma = 3.0$) was convolved with the image to simulate moderate atmospheric scattering, providing a realistic level of spatial degradation.

- **Periodic Noise:** A 2D sinusoidal pattern ($A = 32$, $f = 32$) was added to emulate sensor interference, ensuring visible periodic peaks in the frequency domain:

$$N(x, y) = A \sin\left(2\pi f \frac{x + y}{H + W}\right).$$

- **Low Contrast:** The dynamic range was reduced by attenuating contrast around the image mean with $\alpha = 0.3$, producing a moderate but perceptible loss of visual contrast:

$$I_{\text{low}} = \mu + \alpha(I - \mu).$$

2.2. Frequency Domain Analysis and Filtering

Periodic noise was removed in the frequency domain. The degraded image $I_d(x, y)$ was transformed via the Fast Fourier Transform (FFT), and a symmetric notch (band-reject) filter was applied to suppress noise spikes identified at $(\pm 16, \pm 16)$, as later confirmed by the spectral analysis in Section 3.1:

$$H(u, v) = 1 - \exp\left(-\frac{D(u, v)^2}{2\sigma^2}\right),$$

where $D(u, v)$ is the Euclidean distance from the noise peak. The filter used a rejection radius of $r = 5$ pixels with $\sigma = 3.0$, empirically chosen to remove periodic interference while avoiding excessive attenuation of nearby frequencies. The image was reconstructed using the inverse FFT.

2.3. Wiener Deconvolution for Deblurring

Gaussian blur was addressed using Wiener deconvolution to minimize the mean-square error:

$$\hat{I}(u, v) = \left[\frac{H^*(u, v)}{|H(u, v)|^2 + K} \right] \cdot G(u, v),$$

where $H(u, v)$ is the Fourier transform of the PSF, $G(u, v)$ is the degraded image, and K is the regularization constant (inverse SNR). The PSF was a Gaussian kernel matching the degradation parameters ($11 \times 11, \sigma = 3.0$). K was determined by comparing a variance-based estimation with an empirical grid search maximizing PSNR and SSIM, as detailed in Section 3.3.

2.4. Contrast Enhancement via Adaptive Histogram Equalization

Contrast was enhanced using Contrast-Limited Adaptive Histogram Equalization (CLAHE) to improve local detail without over-amplifying noise, a common issue in global histogram equalization. A clip limit of 2.0 was used to maintain a natural brightness distribution.

2.5. Structural Feature Extraction

To evaluate structural restoration, linear features were extracted from both degraded and restored images. After grayscale conversion, the Canny edge detector (thresholds $T_{\text{low}} = 50, T_{\text{high}} = 150$) was applied. The Probabilistic Hough Transform then detected line segments, which were filtered by requiring a minimum length of 40 pixels and allowing a maximum gap of 15 pixels. The improvement was quantified by comparing the number and continuity of detected lines.

2.6. Pipeline Optimization

The optimal processing order of denoising, deblurring, and contrast enhancement was determined by evaluating multiple configurations. Only physically meaningful sequences were tested to analyze trade-offs between filtering stability and contrast amplification, with detailed comparisons provided in Section 3.2.

3. Results

3.1. Analysis and Frequency Domain Inspection

We analyzed the degraded image in spatial and frequency domains: (1) histogram for contrast compression and (2) FFT for periodic noise localization.

Histogram Analysis. Figure 1(a) presents the intensity histogram of the degraded image. The distribution is tightly concentrated between pixel values of approximately 50–140, indicating a pronounced compression of the dynamic range. This confirms that the applied attenuation factor ($\alpha = 0.3$) successfully simulated a low-contrast condition by suppressing tonal variation while maintaining the global luminance.

Frequency-Domain Inspection. The same image was then transformed into the frequency domain using a two-dimensional Fast Fourier Transform (FFT). As shown in Figure 1(b), the log-scaled magnitude spectrum exhibits distinct symmetric spikes around coordinates $(\pm 16, \pm 16)$ relative to the DC component. These peaks correspond to the artificially introduced sinusoidal interference and are summarized quantitatively in Table 1. The dominant non-DC frequencies have magnitudes of approximately 9.37×10^6 , which are smaller than the DC component yet remain visually prominent in the log-scaled spectrum. These identified coordinates later served as the basis for designing a notch (band-reject) filter for periodic noise suppression.

3.2. Restoration Pipeline

The proposed restoration pipeline was evaluated step-by-step to verify the effectiveness of each component in recovering spatial and perceptual quality. The process begins with the degraded image generated in Section 3.1, which contains three types of degradation: Gaussian blur, periodic noise, and low contrast. Each subsequent stage aims to selectively remove one of these artifacts while maintaining overall structural consistency.

Step 1: Frequency-Domain Filtering. Using the frequency peaks identified at $(\pm 16, \pm 16)$ in the previous analysis, a symmetric notch filter was applied to suppress the corresponding periodic noise. As illustrated in Figure 2(b), the periodic interference was effectively removed from the spectrum, and the reconstructed image exhibited a smooth background without introducing ringing artifacts or edge distortions.

Step 2: Wiener Deconvolution. The denoised image was subsequently deblurred using Wiener deconvolution, with a Gaussian PSF of size 11×11 and $\sigma = 3.0$. The regularization parameter $K = 0.02$ provided a stable trade-off between edge sharpness and noise suppression, resulting in visually crisp structures and well-defined road boundaries. Edges previously smeared by the simulated atmospheric blur were effectively restored, demonstrating the robustness of the deconvolution step.

Step 3: Contrast Enhancement. To recover perceptual visibility and local contrast, Contrast-Limited Adaptive Histogram Equalization (CLAHE) was applied with a clip limit of 2.0. The enhanced image, shown in Figure 2(d), exhibited improved dynamic range and local contrast, particularly in shadowed or low-intensity regions. This stage contributed to more distinct textures and improved edge detection performance in subsequent feature extraction.

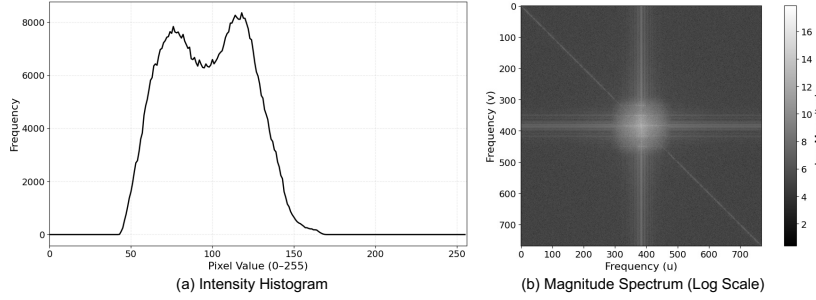


Figure 1. Quantitative analysis of the degraded image. Histogram showing compressed dynamic range (50–140) and FFT magnitude spectrum revealing symmetric periodic noise spikes near $(\pm 16, \pm 16)$.

Table 1. Top frequency peaks in the FFT magnitude spectrum (excluding DC).

Rank	Coord.	Rel.	Mag.
1	(400,400)	(+16,+16)	9.37×10^6
2	(368,368)	(-16,-16)	9.37×10^6
3	(396,384)	(+12,0)	7.01×10^5
4	(372,384)	(-12,0)	7.01×10^5
5	(399,384)	(+15,0)	6.57×10^5



Figure 2. Restoration results at each stage. (a) Degraded input \rightarrow (b) After frequency-domain filtering \rightarrow (c) After Wiener deconvolution \rightarrow (d) After histogram equalization. Each step corresponds to the major restoration stages in the proposed pipeline.

Pipeline Optimization. To determine the optimal order of operations, three pipeline configurations were evaluated:

- **A:** Denoise \rightarrow Deblur \rightarrow Enhance
- **B:** Deblur \rightarrow Denoise \rightarrow Enhance
- **C:** Denoise \rightarrow Enhance \rightarrow Deblur

Each configuration was tested using the same degraded image as input, and evaluated against the ground-truth clean image using PSNR and SSIM metrics. As summarized in Table 2, Configuration (C) achieved the highest quantitative scores (**PSNR = 19.60 dB, SSIM = 0.4699**), indicating that performing enhancement before deblurring helped stabilize the Wiener filter by expanding the image’s tonal range and reducing low-contrast artifacts. Therefore, the remaining experiments adopt Configuration (C) as the default pipeline for subsequent evaluations.

3.3. Quantitative Comparison of K Estimation Methods

To analyze the influence of the Wiener regularization constant K on deblurring performance, two independent estimation approaches were compared. The first was a

Table 2. Quantitative comparison of different pipeline configurations.

Pipeline Order	PSNR (dB)	SSIM
(A) Denoise \rightarrow Deblur \rightarrow Enhance	19.45	0.4675
(B) Deblur \rightarrow Denoise \rightarrow Enhance	19.46	0.4676
(C) Denoise \rightarrow Enhance \rightarrow Deblur	19.60	0.4699

variance-based estimation that analytically computed the noise-to-signal ratio from flat regions of the degraded image, yielding an estimated value of $K_{\text{est}} = 3.6616$. The second approach was an empirical grid search over a wide range ($K \in [10^{-4}, 0.5]$), in which each candidate was evaluated by its PSNR and SSIM with respect to the ground-truth image.

As summarized in Table 3, the variance-based estimate tended to overestimate the noise level, resulting in excessive smoothing during restoration. In contrast, the grid search identified an optimal $K = 0.02$ that achieved the highest PSNR (**19.60 dB**) with competitive SSIM (**0.4699**) under pipeline configuration (C). Although the two estimates differ in magnitude, the grid-searched result effectively balanced noise suppression and edge preservation, indicating

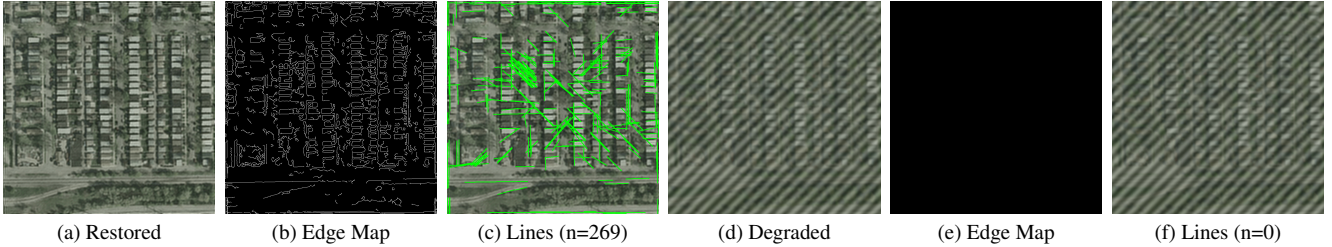


Figure 3. Comparative line detection results between degraded (right) and restored (left) images. Six panels are aligned for compact visual comparison.

that the optimal regularization strength lies in a lower range than the analytical estimate.

Table 3. Comparison between variance-based estimation and grid-searched K values (evaluated with pipeline (C)).

Method	K	PSNR (dB)	SSIM
Variance-based estimation	3.6616	9.39	0.1191
Grid search (sub-optimal)	0.0100	19.59	0.4746
Grid search (optimal)	0.0200	19.60	0.4699

In conclusion, the variance-based analytical estimation provides a physically interpretable but overly conservative regularization level, while the grid search empirically refines it to a more effective operating point. Hence, $K = 0.02$ was adopted as the default value for subsequent experiments due to its superior balance between deblurring stability and noise suppression, as it achieved the highest PSNR and consistently stable performance across all pipeline configurations.

3.4. Structural Feature Extraction and Quantitative Analysis

To evaluate how effectively the proposed restoration pipeline recovered structural information, the restored image was analyzed using edge and line detection techniques. The goal is to extract meaningful geometric features—such as road boundaries, orientations, and intersections—from the restored aerial image.

Edge and Line Detection. A Canny Edge Detector was applied to the restored image to highlight structural boundaries while suppressing residual noise. Subsequently, the Probabilistic Hough Transform was used to detect straight road segments based on these edge features. As shown in Figure 3, the degraded image failed to produce valid edges or lines due to blur and periodic interference, resulting in zero detected line segments. In contrast, the restored image successfully revealed the road network, detecting **269 linear features** that align well with the true road boundaries.

This demonstrates a substantial improvement in geometric clarity following restoration.

Orientation Distribution. The detected lines were converted into their angular representations to analyze the dominant road orientations. As shown in Figure 4, the histogram of line angles exhibits distinct peaks near **0°**, **45°**, **90°**, and **135°**, indicating a strong grid-like urban layout. The mean line orientation was measured as **77.32°** with a standard deviation of **61.30°**, showing that the road network primarily consists of orthogonal and diagonal structures. This angular distribution quantitatively supports the visual impression of a structured, rectilinear road network.

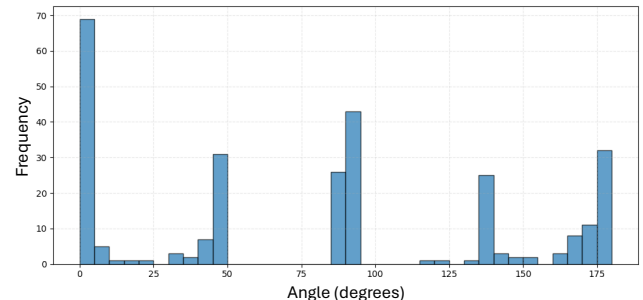


Figure 4. Histogram of detected line orientations in the restored image. Distinct angular peaks at **0°**, **45°**, **90°**, and **135°** reflect a grid-like urban structure.

Road Density and Intersection Estimation. The spatial density of detected road lines was computed as the total length of detected line segments (in pixels) divided by the image area (in pixels²), yielding a linear density of **0.0367 px/px²**. This quantity reflects line-length per unit area (not an area fraction). Additionally, intersections were identified by locating crossing points between detected line segments, resulting in **288 intersections** (Figure 5). These intersections correspond to major road crossings or block separations, further validating that the restored image successfully recovers the geometric layout of the urban scene.



Figure 5. Intersection map showing detected crossing points (red dots) on the restored image. A total of 288 intersections were identified, indicating restored road connectivity and continuity.

To further comply with the assignment requirement of analyzing a specific region, road density was additionally computed for a centered 512×512 region of interest (ROI), defined as $(x_{\min}, y_{\min}, x_{\max}, y_{\max}) = (\frac{W}{2} - 256, \frac{H}{2} - 256, \frac{W}{2} + 256, \frac{H}{2} + 256)$. A line segment was counted if it was located within or intersected the ROI, and its full length was added to the total line length for simplicity. The resulting ROI-based density was **0.0489 px/px²**, which is higher than the global average (**0.0367 px/px²**), indicating that the central urban block exhibits a denser road network. This ROI analysis eliminates potential border artifacts and provides a more representative estimate of road structure density.

4. Discussion & Conclusion

The proposed restoration pipeline effectively reconstructs both the spatial and perceptual quality of degraded aerial imagery through a sequence of physically interpretable operations. Each component—frequency-domain filtering, Wiener deconvolution, and adaptive histogram equalization—was designed to target a specific degradation source while maintaining global consistency. The stepwise evaluation confirmed that the method successfully removes periodic noise, recovers structural sharpness, and restores contrast balance, resulting in a significant improvement in both visual clarity and quantitative metrics.

From a quantitative perspective, the optimized configuration (**C: Denoise → Enhance → Deblur**) achieved the highest fidelity, with **PSNR = 19.60 dB** and **SSIM = 0.4699**, outperforming alternative orders. Structural analysis further validated the method’s effectiveness: the number of detected linear features increased from 0 to 269, and 288 intersections were identified in the restored image. These results demonstrate that the proposed pipeline not only enhances

low-level pixel information but also enables the recovery of higher-level geometric features such as road continuity and connectivity.

Despite its strong performance, several limitations remain. First, the Wiener filter relies on a manually tuned regularization constant ($K = 0.02$), which may not adapt well to different blur and noise conditions. Second, while the notch filter effectively removes periodic interference, its parameters (radius r and bandwidth σ) were selected empirically, limiting adaptability to more complex noise spectra. Finally, the histogram equalization stage, though effective for local contrast enhancement, can introduce mild over-amplification in uniform regions if the clip limit is not carefully chosen.

Future extensions of this work may include adaptive parameter estimation, where filter parameters and K values are dynamically determined based on local image statistics or noise estimation models. Additionally, deep learning–based restoration methods could be integrated into the pipeline to further improve generalization across diverse conditions. Finally, expanding the evaluation to larger urban datasets and incorporating real-world sensor noise models would allow for more robust and scalable validation.

In summary, the proposed restoration and analysis framework achieves a clear balance between interpretability and performance. Through explicit modeling of degradation processes and systematic parameter justification, it provides a transparent yet effective approach to aerial image restoration—recovering both visual fidelity and geometric structure in a manner that is physically grounded and analytically verifiable.